ACS NANO

www.acsnano.org

ARTICLE

PEGylated Ultrasmall Iron Oxide Nanoparticles as MRI Contrast Agents for Vascular Imaging and Real-Time Monitoring

Kuan Lu,[#] Ruru Zhang,[#] Hongzhao Wang, Cang Li, Zhe Yang, Keyang Xu, Xiaoyi Cao, Ning Wang, Wu Cai,[*] Jianfeng Zeng,[*] and Mingyuan Gao[*]

Cite This: *ACS Nano* 2025, 19, 3519−3530

Read Online

ACCESS | Metrics & More | Article Recommendations | Supporting Information

ABSTRACT: **Accurate imaging evaluations of pre- and post-treatment of cardiovascular diseases are pivotal for effective clinical interventions and improved patient outcomes. However, current imaging methods lack real-time monitoring capabilities with a high contrast and resolution during treatments. This study introduces PEGylated ultrasmall iron oxide nanoparticles (PUSIONPs), which have undergone comprehensive safety evaluations, boasting an r_1 value of 6.31 mM^{-1} s^{-1}, for contrast-enhanced magnetic resonance angiography (MRA). Systematic comparisons against common clinical methods in rabbits reveal that PUSIONPs-enhanced MRA exhibited improved vascular contrast, clearer vascular boundaries, and superior vessel resolution. Moreover, owing to their nanosize, PUSIONPs demonstrate significantly prolonged blood circulation compared to small molecular contrast agents such as Magnevist and Ultravist. This extended circulation enables captivating real-time monitoring of thrombolysis treatment for up to 4 h in rabbit models postsingle contrast agent injection. Additionally, in larger animal models such as beagles and Bama minipigs, PUSIONPs-enhanced MRA also showcases superior contrast effects, boundary delineation, and microvessel visualization, underscoring their potential to transform cardiovascular imaging, particularly in real-time monitoring and high-resolution visualization during treatment processes.**

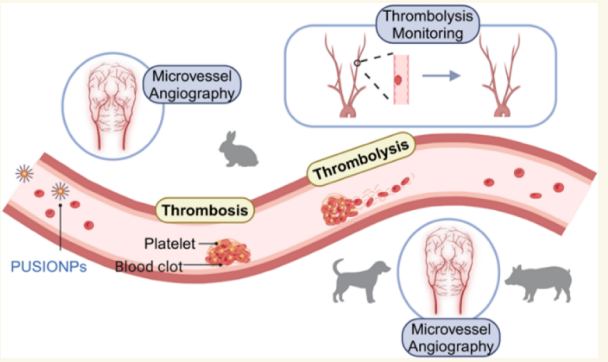

KEYWORDS: *iron oxide nanoparticles, magnetic resonance angiography, contrast agent, thrombolysis monitoring, cardiovascular diseases*

1. INTRODUCTION

Cardiovascular diseases (CVDs) pose an immense global health challenge due to their alarming rates of morbidity, mortality, and disability.[1−5] Among the spectrum of CVDs, ischemic disorders such as thrombosis are particularly prevalent.[6] Thrombolysis using recombinant tissue plasminogen activator stands as a primary treatment approach for intravenous thrombolysis.[7] However, patients subjected to thrombolysis often confront the distressing recurrence of episodes, highlighting the imperative for continuous real-time monitoring of their condition.[8] Furthermore, the pivotal role of imaging assessments, before and after treatment, cannot be overstated. These assessments serve as indispensable guides in formulating clinical treatment strategies and ultimately improving patient outcomes.[9] Therefore, the pursuit of precise diagnosis, effective intervention, and vigilant real-time monitoring remains paramount in the relentless battle against these life-threatening cardiovascular conditions.

Conventional methods for assessing blood vessels encompass a range of imaging techniques including ultrasound (US),[10,11] computed tomography angiography (CTA),[12,13] digital subtraction angiography (DSA),[14,15] and magnetic resonance angiography (MRA).[14,16] Each of these methods has its own set of advantages and limitations in the context of CVD assessment. US, notable for its ease of use and lack of radiation exposure, offers accurate localization of lesions, assessment of luminal narrowing, and dynamic visualization of blood flow.[1,17] However, its spatial resolution is relatively low, and it can be challenging to perform examinations in areas with total ultrasound wave reflection or severe acoustic wave

Received: September 22, 2024
Revised: December 10, 2024
Accepted: December 18, 2024
Published: January 17, 2025

attenuation, such as the lungs, gastrointestinal tract, or dense bone tissues. Additionally, in severely obese patients, the presence of a thick subcutaneous fat layer can increase background noise in the images, potentially impacting diagnostic accuracy.[18] CTA is another widely utilized method for evaluating CVDs, offering high spatial and density resolutions and ease of use. However, it is susceptible to the partial volume effect, which can affect accurate assessment of luminal stenosis in the presence of calcified plaque in vessel walls. Additionally, bone artifacts can interfere with the visualization of blood vessels located near bone structures.[19] Furthermore, CTA involves exposure to ionizing radiation, and the use of contrast agents may have detrimental effects on renal function.[20] DSA stands out as a dynamic imaging technique that allows real-time observation of target vessels and enables concurrent interventional procedures, such as stent placement, based on imaging guidance. It is often regarded as the "gold standard" for diagnosing vascular diseases.[15] Nevertheless, DSA is an invasive procedure associated with a degree of radiation exposure, and it necessitates a potentially traumatic femoral artery puncture for contrast agent administration.[21] In contrast, MRA offers a noninvasive means of assessing vascular anatomy and hemodynamics. By reconstructing volumetric data through multiplanar techniques, MRA can produce angiograms comparable to those generated by invasive methods such as DSA.[22] Importantly, MRA eliminates the risks associated with arterial catheterization, iodinated contrast agents, and exposure to ionizing radiation, making it a safer option for patients.[23]

In clinical MRA, two primary categories are commonly employed: time-of-flight MRA (TOF-MRA) and contrast-enhanced MRA (CE-MRA).[24] TOF-MRA, an MRI technique, is tailored for visualizing blood flow within vessels without the need for administering a contrast agent. This method relies on the intrinsic enhancement of spins as they traverse an imaging slice.[25] However, it is crucial to acknowledge the inherent limitations associated with TOF-MRA. In cases of slow blood flow or when blood flows parallel to the imaging plane of a vessel, it can become saturated, resembling stationary tissue, and this can result in signal loss from the vessel of interest.[26] Turbulent blood flow can induce spin-dephasing and unexpectedly short transverse relaxation times (T2), further contributing to signal loss within the vessel. Additionally, TOF-MRA typically necessitates relatively extended acquisition times, a factor that may potentially limit its clinical utility in specific scenarios.

CE-MRA operates on the principle of utilizing a contrast agent to reduce the longitudinal relaxation time ($T1$) within blood vessels, thereby enhancing the contrast of the surrounding tissue and improving vascular imaging.[27,28] The application of the 3D-FLASH sequence in CE-MRA scans leads to a shortened repetition time (TR), resulting in faster imaging when compared to TOF-MRA.[29] Traditionally, gadolinium-based contrast agents, exemplified by Magnevist, have served as the primary choice for clinical MR contrast agents for over three decades. However, these Gd-based contrast agents are associated with potential risks such as nephrogenic systemic fibrosis and brain deposition.[30−32] Furthermore, due to their limited circulation half-life within the bloodstream, Gd-based contrast agents must be administered for each CE-MRA procedure to facilitate real-time disease assessment.[33,34] This practice places an increased physical and economic burden on patient. To address these challenges, there is a pressing need to develop innovative contrast agents that can offer improved safety and efficacy in CE-MRA procedures.

In recent years, ultrasmall iron oxide nanoparticles (USIONPs) have emerged as a prominent contender in the realm of MRI contrast agents.[35,36] They offer a plethora of advantages over conventional Gd-based agents, including their exceptional magnetic properties, prolonged blood half-life, and impeccable biocompatibility.[37−40] The application of USIONPs as T1 contrast agents has yielded significant outcomes in various preclinical studies.[41−44] For instance, Wang et al. conducted vascular imaging assessments in SD rats, harnessing the power of USIONPs at a 7.0 T field strength alongside SWI technology. This innovative approach facilitated the clear visualization of cerebral blood vessels, even those with diameters as diminutive as 10 μm.[45] In another notable study, Wei et al. highlighted both the biocompatibility and impressive vascular imaging capabilities of USIONPs in rats within 60 min postinjection.[46] Furthermore, Lu et al. harnessed the potential of USIONPs for MRA in a model of middle cerebral artery occlusion in both beagle dogs and rhesus monkeys, achieving exceptional imaging results.[47] These investigations undeniably showcase the substantial potential of USIONPs as a superior contrast agent for T1 MRI of blood pools, holding promise for eventual clinical application. However, despite these encouraging findings, it is essential to acknowledge that they do not fully address the genuine clinical needs for real-time, precise, and extended monitoring of emergency thrombolysis patients with CVDs.

In this study, we meticulously compared the imaging efficiency of CE-MRA using PEGylated ultrasmall iron oxide nanoparticles (PUSIONPs), CE-MRA with Magnevist, TOF-MRA, and CTA employing Ultravist. Our investigation commenced with the systematic imaging of the head and neck vasculature in rabbits, revealing the exceptional potential of PUSIONPs as blood pool contrast agents. Building upon these promising results, we established a robust model to replicate the thrombolysis process. This monitoring phase unveiled the notable capability of PUSIONPs to sustain vascular imaging for extended durations, providing an effective means of detecting thrombosis within blood vessels. Furthermore, we extended our research to include beagle dogs and Bama minipigs to validate the efficacy of PUSIONPs as MR T1 blood pool contrast agents and to explore their potential for clinical translation. Our findings demonstrate that PUSIONPs serve as highly effective MRI contrast agents for real-time thrombolysis monitoring, significantly reducing the need for repeated contrast agent administration and marking a significant advancement in cardiovascular imaging and diagnosis.

2. RESULTS AND DISCUSSION

2.1. Characterization of PUIONPs. The PUSIONPs utilized in this study were produced by Suzhou Xinying Biomedical Technology Co., Ltd. These nanoparticles were synthesized using a high-temperature thermal decomposition method and have undergone comprehensive safety evaluation studies involving SD rats and beagle dogs, demonstrating excellent biocompatibility. Representative TEM images, as illustrated in Figure 1a, showcase the uniform distribution of the PUIONPs. Statistical analysis of the particle size affirmed excellent monodispersity, with an average size of 3.1 ± 0.5 nm (Figure 1b). Dynamic light scattering (DLS) analysis revealed

https://doi.org/10.1021/acsnano.4c13356
ACS Nano 2025, 19, 3519−3530

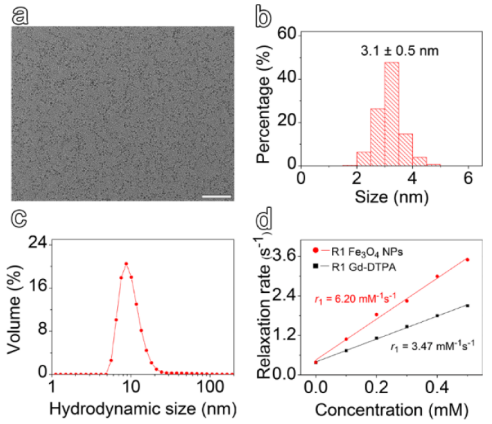

Figure 1. (a) Representative TEM images of PUSIONPs and (b) their size histogram (scale bar = 100 nm). (c) Hydrodynamic size of PUSIONPs determined based on DLS. (d) R_1 relaxivities of PUSIONPs and Gd-DTPA as a function of the Fe concentration.

a narrow hydrodynamic size distribution profile for PUSIONPs, with a peak at approximately 9 nm (Figure 1c). Furthermore, it was determined that the longitudinal relaxivity of the PUSIONPs at 3.0 T is 6.20 mM^{-1} s^{-1}, which is nearly double the value of 3.47 mM^{-1} s^{-1} measured for the Magnevist under the same conditions (Figure 1d). These results suggest that PUSIONPs demonstrate significantly superior MRI contrast enhancement performance and are expected to outperform Magnevist in the context of MRA.

2.2. Evaluation of MRA in Rabbits. Expanding upon the impressive *in vitro* MRI capabilities of PUSIONPs, we conducted a systematic comparison of imaging efficiency involving CE-MRA with PUSIONPs (CE-MRA (Fe)), CE-MRA with Magnevist (CE-MRA (Gd)), CTA with Ultravist, and TOF-MRA in rabbits, utilizing clinical facilities. For CE-MRA, MR images of the head and neck were acquired both before and at various time points (3 min, 1 h, 2 h, and 4 h) after the administration of

PUSIONPs (Figure 2a) or Magnevist (Figure 2b). Notably, delineating the distribution of blood vessels in rabbits presented challenges before the administration of these contrast agents. Following the administration of 0.1 mmol/kg of PUSIONPs or Magnevist, both exhibited significant enhancement in the measured vessels during the initial phase.

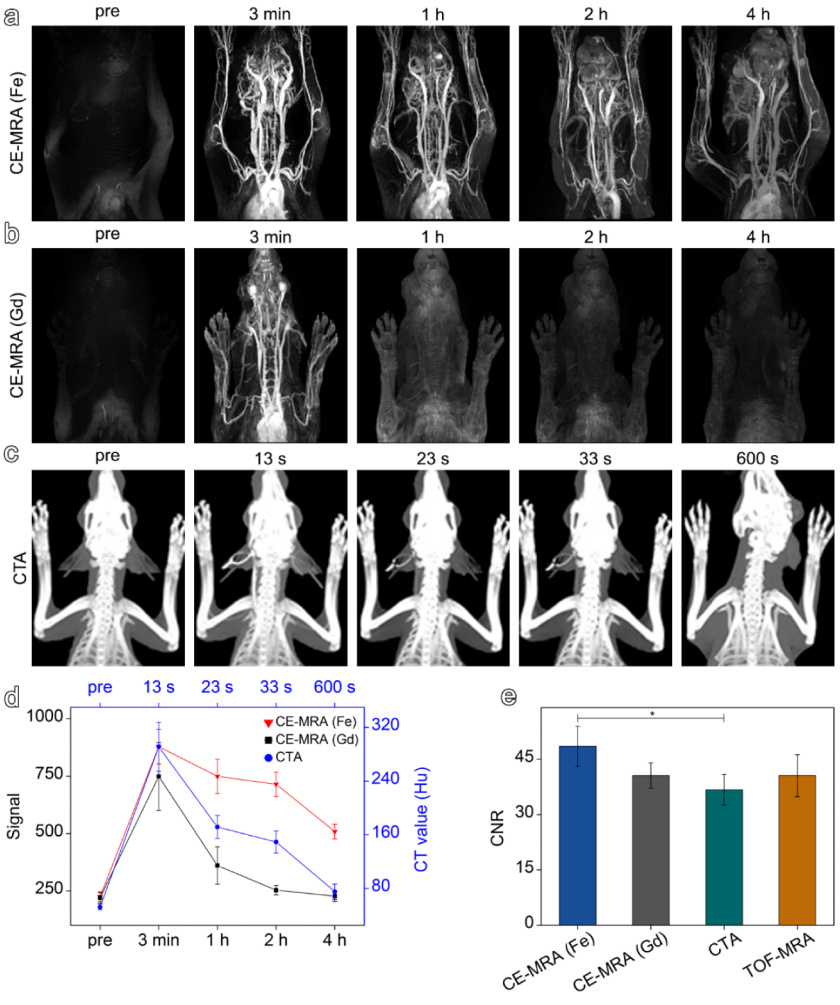

Figure 2. (a) CE-MRA images of healthy rabbits before and after intravenous injections of PUSIONPs and (b) Gd-DTPA at different time points. (c) CTA images of healthy rabbits before and after intravenous injections of Ultravist at various time points. (d) Plot of MRI signal/CT value enhancement versus time for PUSIONPs, Gd-DTPA, and Ultravist. The strong MRI signal of the PUSIONPs lasted longer than that of Gd-DTPA and Ultravist. (e) CNR measured in the carotid common artery of normal rabbits with CE-MRA (Fe), CE-MRA (Gd), CTA, and TOF-MRA.

https://doi.org/10.1021/acsnano.4c13356
ACS Nano 2025, 19, 3519−3530

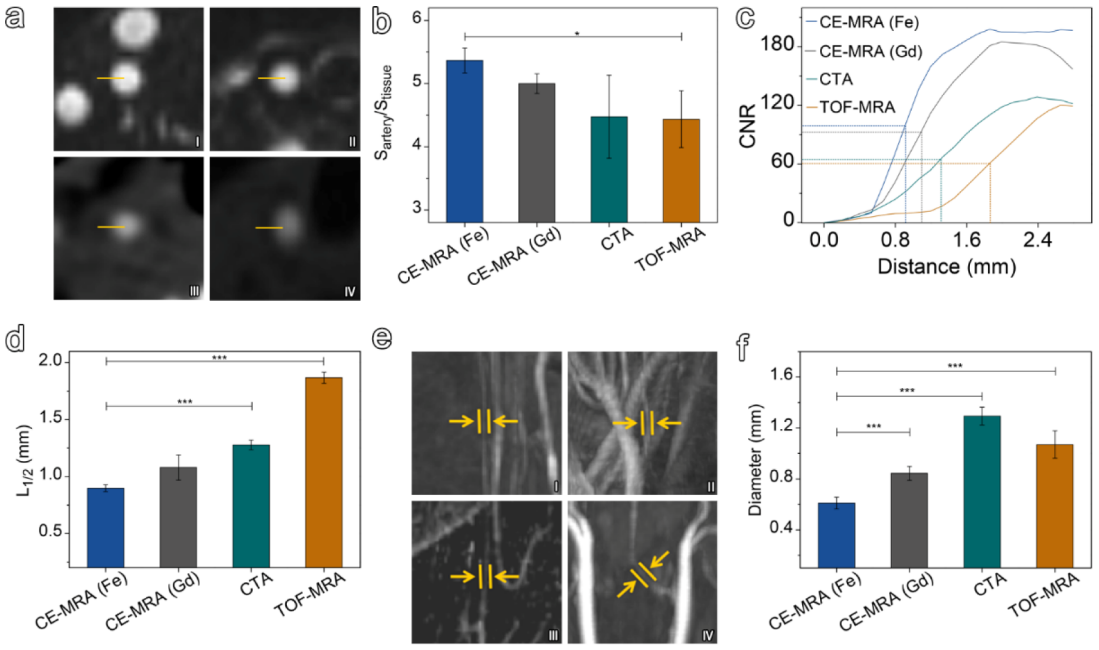

Figure 3. (a I–IV) Transverse CE-MRA (Fe), CE-MRA (Gd), and CTA and TOF-MRA images in the same position of the ipsilateral carotid common artery in rabbits. (b) Signal ratio between the carotid common artery and surrounding tissue for the above four imaging methods. (c) Analysis curve from ImageJ software corresponding to (a). (d) The distance needed for the signal of the four imaging techniques in (a) to achieve half of the maximum CNR. (e I–IV) The smallest vessels shown by CE-MRA (Fe), CE-MRA (Gd), CTA, and TOF-MRA, respectively. (f) Quantitative values of the smallest vessel diameters that can be displayed by four imaging modalities.

However, as time progressed, rabbits injected with Magnevist rapidly lost their vascular signals, with no discernible signals after 1 h. In contrast, rabbits injected with PUSIONPs still displayed clear vascular imaging, even after 4 h. Due to the faster scan time of CT compared to MRI, CTA imaging was performed at 13 s, 23 s, 33 s, and 600 s after Ultravist injection at a dosage of 1 mL/kg, as depicted in Figure 2c. It is evident that the MIP images of the vessels in the CTA were significantly affected by bone artifacts. This issue could potentially be mitigated through volume rendering, as demonstrated in Figure S1. However, the imaging performance of CTA falls short of CE-MRA, and the contrast enhancement rapidly diminishes after administration, with virtually no enhancement remaining by 10 min. Further quantification of vascular signals indicated that the signals for all three contrast-enhanced imaging techniques increased significantly after injection and then gradually declined (Figure 2d). Notably, the signal from PUSIONPs exhibited a significantly slower decline compared to Magnevist and Ultravist, attributed to their extended blood half-life of 3.28 h (Figure S2). Notably, vascular structures remained clearly distinguishable even 4 h postcontrast, despite the gradual reduction in contrast intensity within the blood vessels. TOF-MRA, which does not require a contrast agent and acquires only one image, as shown in Figure S3, can display the larger arteries in the rabbit's head and neck. However, it lacks the level of detail seen in CE-MRA. The results presented in Figure 2e reveal that the maximum CNR values of the carotid common artery using the aforementioned four methods were 48.5 ± 5.5, 40.8 ± 3.5, 36.8 ± 4.2, and 40.6 ± 5.6. These findings validate the high contrast enhancement capabilities of PUSIONPs.

To comprehensively evaluate the imaging performance of various techniques, we conducted quantitative analyses from multiple perspectives, including contrast, vascular boundary clarity, and resolution. When transverse images of the carotid common artery were compared using the four different imaging methods, all techniques showed improved visibility of blood vessels, with similar vessel diameters (Figure 3a). Notably, CE-MRA (Fe) stood out among the four techniques. As depicted in Figure 3b, the signal ratio of the artery to the surrounding tissue in CE-MRA (Fe) was 7.3% higher than that in CE-MRA (Gd), 19.9% higher than that in CTA, and 21.0% higher than that in TOF-MRA. This suggests that CE-MRA (Fe) provided the most promising contrast for vascular imaging.

Furthermore, the vascular boundaries delineated by CE-MRA (Fe) were significantly sharper than those obtained with other imaging techniques, as shown in Figure 3c. When using the distance to reach half of the maximum CNR value (referred to as $L_{1/2}$) to quantitatively describe vascular boundary clarity, as shown in Figure 3d, the $L_{1/2}$ along the orange line across the artery in Figure 3c was 0.91, 1.01, 1.27, and 1.87 mm for CE-MRA (Fe), CE-MRA (Gd), CTA, and TOF-MRA, respectively. Quantitative analysis results indicated that CE-MRA is the optimal method for displaying vascular boundaries. This superior performance can be attributed to MRI's high soft tissue contrast and the high relaxation rate of PUSIONPs. The exceptional ability to visualize vascular boundaries suggests that CE-MRA is more effective at illustrating fine details of blood vessels.

To assess the capability of imaging microvessels, we analyzed the MIP reconstruction images obtained using the four imaging techniques mentioned above. The results in Figure 3e demonstrated that CE-MRA (Fe) could identify vessels with significantly smaller diameters than the other three methods. The smallest diameters that were clearly visible for the four methods were approximately 0.61 ± 0.05, 0.84 ± 0.06, 1.29 ± 0.08, and 1.07 ± 0.11 mm (Figure 3f). These findings highlight the excellent angiography performance of PU-SIONPs, with CE-MRA (Fe) enabling the observation of

https://doi.org/10.1021/acsnano.4c13356
ACS Nano 2025, 19, 3519–3530

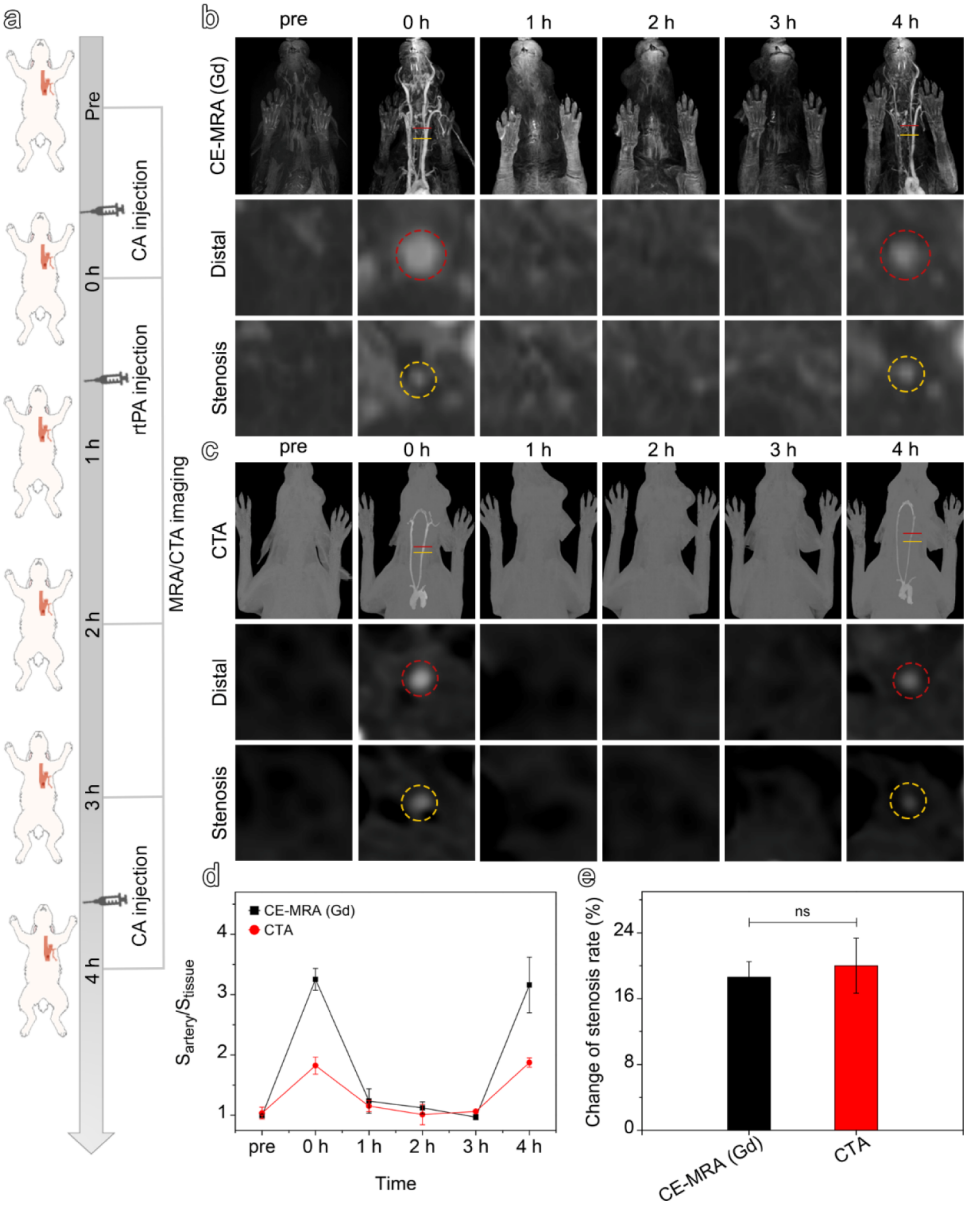

Figure 4. (a) Schematic illustration of imaging in the thrombolysis process. (b) MIP images of the thrombolysis process and axial MR images of the distal normal and stenosis vessel after injection of Gd-DTPA (c) Ultravist. (Note: red solid and dotted lines indicate distal normal vessel; yellow solid and dotted lines indicate stenosis vessel, where the thrombus was located.) (d) Graph of the arterial-to-tissue signal ratio in a model vessel over time for thrombolysis monitoring. (e) The change in stenosis rate after thrombolysis for 4 h.

higher vascular contrast, greater vascular boundary clarity, and superior vessel resolution. More importantly, the extended duration of PUSIONPs-enhanced MRA aligns well with the requirements of real-time observation for clinical thrombolytic treatment, which typically spans 1 to 2 h.

2.3. Monitoring Rabbit Carotid Thrombolysis. To assess the potential application of PUSIONPs in thrombolysis monitoring, the rabbit carotid artery thrombosis models were first established by wrapping the carotid artery with filter paper soaked in 10% $FeCl_3$ for 20 min (Figure S4a). Confirmation of the model's success was achieved by extracting the carotid common artery at the induction point for H&staining. Pathological sections, viewed at 100× and 400× magnification, confirmed the presence of a mixed thrombus composed of red blood cells, inflammatory cells, and fibrin (Figure S4b). This kind of thrombus could be dissolved by recombinant tissue plasminogen activator (rt-PA).

After successfully constructing the model, the degree of carotid artery stenosis was first assessed using TOF-MRA. The models with similar degrees of stenosis were selected for

further experiments. Subsequently, rt-PA was administered through the auricular vein, and thrombolysis was monitored at different time points using various imaging methods aforementioned (Figures 4a and 5a). Figure 4b,c provide the imaging assessment results of the thrombolysis process using CE-MRA (Gd) and CTA, respectively. As can be seen, both techniques exhibited a rapid increase in the signal upon contrast agent administration. However, due to their rapid metabolism, the signal declined quickly, which inadequately reflected the thrombolytic process in the vessels. Therefore, contrast agents were reinjected after 4 h to monitor the

https://doi.org/10.1021/acsnano.4c13356
ACS Nano 2025, 19, 3519−3530

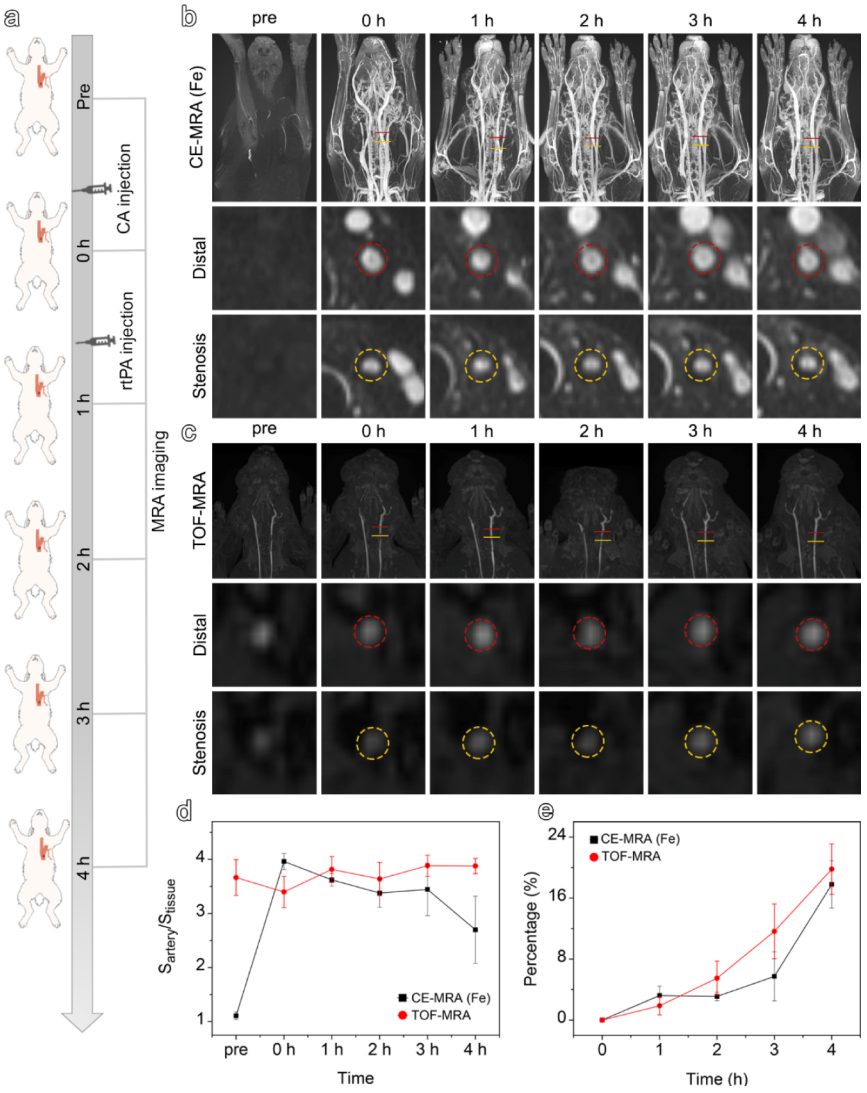

Figure 5. (a) Scheme for the *in vivo* imaging study of thrombolysis progression in CE-MRA (Fe) and TOF-MRA. (b) MIP images of the thrombolysis process and axial MR images of the stenosis and distal normal vessel in CE-MRA (Fe) and (c) TOF-MRA. (Note: red solid and dotted lines indicate distal normal vessel; yellow solid and dotted lines indicate stenosis vessel, where the thrombus was located.) (d) Curve of the ratio of arterial to surrounding tissue signal of the model vessel of thrombolysis monitoring with time. (e) Change in stenosis rate at each time point after thrombolysis.

thrombolytic effect. For the analysis of imaging performance, the signal ratio of the artery to the surrounding tissue was used as a reference. As shown in Figure 4d, the ratios of the two imaging techniques peaked immediately after contrast agent administration (0 h), then maintained a steady value around 1 and were restored following the second injection at 4 h. For evaluating thrombolytic efficacy, the alteration in the stenosis ratio was adopted as a benchmark. As illustrated in Figure 4e, the change rates obtained by both imaging methods were almost identical, providing a clear measurement of lumen stenosis following the second injection. Nevertheless, the multiple contrast agent injections made it impractical to track the

course of thrombolytic therapy in live scenarios, as contrast agents would need to be readministered for each blood vessel examination, increasing the incidence of contrast agent-related side effects and also the economic costs. In addition, both Magnevist and Ultravist contrast agents were found to leak from the blood vessels rapidly after injection. This led to an increase in whole-body signal while decreasing the contrast between blood vessels and the surrounding tissue background, making it more challenging to distinguish blood vessels.

Next, we observed the thrombolytic process of the carotid thrombus by using PUSIONPs. The results in Figure 5b showed that, in contrast to Magnevist, the clinically used contrast agent, PUSIONPs were able to maintain the enhancement effect over an extended period. The carotid artery remained well visualized at all subsequent time points following a single injection of the PUSIONPs. In addition, TOF-MRA, despite not requiring a contrast agent, can also effectively monitor the thrombolysis process in real-time using specific sequences, as illustrated in Figure 5c. This contrast-agent-free approach results in minimal fluctuations in both the carotid signal and the signal from the surrounding tissue over time. Quantitative analysis demonstrated that the signal ratio of the carotid artery to surrounding tissue in CE-MRA (Fe) and TOF-MRA remained at a high signal level for an extended period, providing additional confirmation of prolonged and

https://doi.org/10.1021/acsnano.4c13356
ACS Nano 2025, 19, 3519−3530

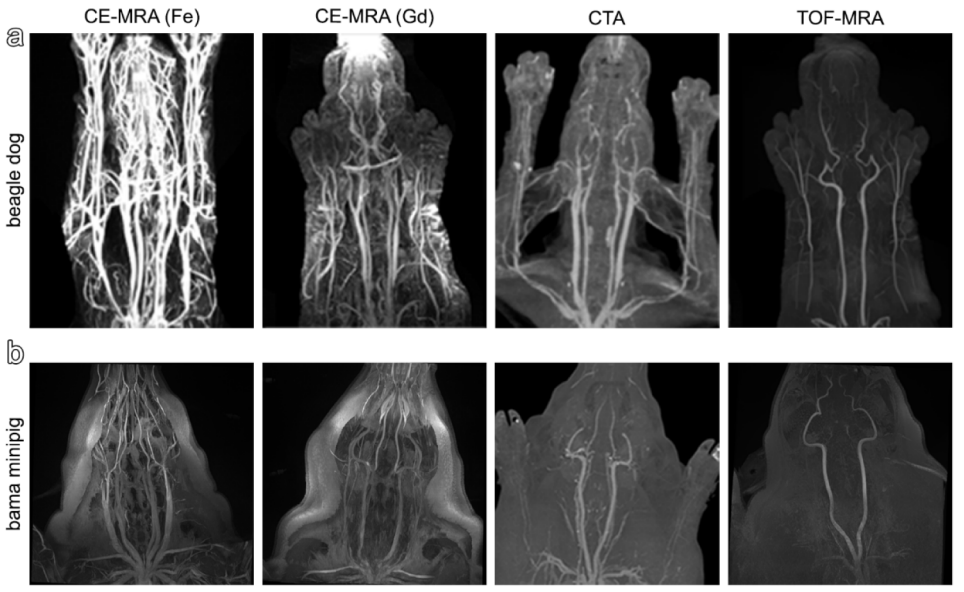

c

	beagle dog				bama minipig			
	CE-MRA (Fe)	CE-MRA (Gd)	CTA	TOF-MRA	CE-MRA (Fe)	CE-MRA (Gd)	CTA	TOF-MRA
S_{artery}/S_{tissue}	6.75 ± 0.39	2.64 ± 0.28	1.90 ± 0.08	3.95 ± 0.21	7.80 ± 1.83	6.93 ± 1.37	5.19 ± 0.43	3.07 ± 0.38
$L_{1/2}$ (mm)	0.75 ± 0.10	0.97 ± 0.11	0.88 ± 0.15	1.06 ± 0.16	0.91 ± 0.12	1.10 ± 0.13	1.44 ± 0.10	1.23 ± 0.12
Diameter (mm)	0.89 ± 0.16	1.29 ± 0.23	1.39 ± 0.20	1.17 ± 0.12	0.70 ± 0.11	0.83 ± 0.11	1.12 ± 0.10	0.93 ± 0.10

Figure 6. MIP images of healthy beagle dogs (a) and Bama minipigs (b) in four imaging modalities. (c) Contrast, vascular boundary clarity, and resolution of four imaging methods. Note: S_{artery}/S_{tissue} refers to signal ratio between the common carotid artery and surrounding tissue; $L_{1/2}$ refers to the distance required for the signal of the four imaging techniques in Figure S6a,d to achieve half of the maximum CNR value. Diameter refers to the tiniest vessels shown in four imaging ways.

accurate visualization of blood vessels (Figure 5d). According to the imaging results, the evolution of the stenosis rate over time was calculated and plotted in Figure 5e, showing that both techniques were competent in assessing trends in carotid stenosis rate at different intervals over a 4-h period. Nevertheless, from a radiological perspective, CE-MRA (Fe) offers a noticeably clearer display of blood vessels compared to TOF-MRA, making it easier to monitor thrombolysis in tiny blood vessels.

Moreover, when assessing a carotid artery that was completely occluded in a particular location, TOF-MRA failed to provide a complete visualization of the vessel or lesion site as CE-MRA did (Figure S5a). Additionally, TOF-MRA may overestimate the severity of stenosis

in vessels that were significantly narrowed compared to those of CE-MRA (Figure S5b). The reason for this discrepancy was that CE-MRA (Fe) was less reliant on blood inflow or phase-shift effects, reducing the influence of motion- and flow-related artifacts and leading to substantially increased image resolution. Compared to TOF-MRA, CE-MRA (Fe) provided a more precise evaluation of severely narrowed vessels, avoiding overestimation, could accurately pinpoint the location of obstructions in completely occluded vessels. Furthermore, CE-MRA (Fe) demonstrates superior time efficiency compared to TOF-MRA, making it the unequivocal choice for critically ill patients.

Table S1 summarizes the change in stenosis rate obtained by the four methods after 4 h of thrombolysis, revealing no significant differences among the mentioned approaches. However, the above results from *in vivo* imaging of the carotid thrombosis model strongly indicate that PUSIONPs have substantial potential as outstanding contrast agents for MR angiography. It is important to note that their hydrodynamic size, approximately 9 nm, restricts PUSIONPs from freely passing through the intercellular gaps in the vascular wall. This, coupled with their high relaxivity, greatly enhances the contrast between blood vessels and the surrounding tissues. Consequently, it becomes possible to achieve high-resolution MR angiography of microvasculature and vascular disorders. More importantly, the prolonged blood half-life of PUSIONPs facilitates extended monitoring of the treatment process with just a single injection, offering an extended window for observation.

2.4. MRA in Beagle Dogs and Bama Minipigs. Large animal experiments are crucial in evaluating material effectiveness and their translation to clinical use. After validating PUSIONPs' capacity for imaging vessels in rabbits, we extended our study to explore their application in visualizing vessels in beagle dogs and Bama minipigs through head and neck angiography using CE-MRA (Fe), CE-MRA (Gd), CTA, and TOF-MRA at various intervals (Figure S6). Upon administration of both PUSIONPs and Magnevist, a noticeable upsurge in the vascular signals was observed. However, while Magnevist signals declined rapidly over time, PUSIONPs sustained signals even after 4 h, facilitating robust vessel

visualization. CTA improved vascular signals post-Ultravist administration but lost the signal at 10 min due to rapid

https://doi.org/10.1021/acsnano.4c13356
ACS Nano 2025, 19, 3519−3530

metabolism. Quantitative analysis revealed rapid signal enhancement, followed by gradual attenuation, with PUSIONPs displaying the most effective prolonged signal maintenance and minimal amplitude attenuation (Figure S7). CE-MRA (Fe) notably excelled in vascular imaging, evident in amplified vascular contrast and enhanced vasculature visualization in Figure 6a,b.

Subsequently, quantitative analysis was undertaken to evaluate its efficacy in enhancing image contrast, displaying vessel boundaries, and visualizing microvessels in beagle dogs and Bama minipigs. In the case of beagle dogs, cross-sectional images from four methods were extracted for analysis, showing a clearly outlined lumen across all four methods, with CE-MRA (Fe) demonstrating the most distinctive delineation (Figure S8a). The signal ratios of first-pass phase vessels to surrounding tissue highlighted CE-MRA (Fe) as providing significantly stronger contrast of 6.75 ± 0.39, approximately 156%, 255%, and 71% higher than CE-MRA (Gd), CTA, and TOF-MRA, respectively (Figure 6c). Moreover, an evaluation was conducted to assess the ability to define vessel boundaries, echoing the observations in the rabbit model, where CE-MRA (Fe) exhibited the sharpest curve (Figure S8b). The $L_{1/2}$ values for CE-MRA (Fe), CE-MRA (Gd), CTA, and TOF-MRA were 0.75 ± 0.10, 0.97 ± 0.11, 0.88 ± 0.15, and 1.06 ± 0.16 mm, respectively (Figure 6c). Additionally, the diameters of the smallest visible vessels were 0.89 ± 0.16, 1.29 ± 0.23, 1.17 ± 0.12, and 1.39 ± 0.20 mm for the four methods, respectively (Figures S8c and 6c). These findings highlight the outstanding potential of CE-MRA (Fe) in visualizing small vessels.

Likewise, cross-sectional images of the carotid artery in pigs at the corresponding level were analyzed to ascertain the vessel-to-surrounding-tissue signal ratio, the ability to display vessel boundaries, and the smallest visible vessel, contributing to an assessment of their visualization capacity (Figure S8d–f). These outcomes corroborate previous findings, illustrating the notable imaging capabilities of the CE-MRA methods. The quantitative data in Figure 6c depicted that CE-MRA (Fe) exhibited the highest signal ratio between the artery and surrounding tissue (7.80 ± 1.83), the clearest vessel boundaries ($L_{1/2}$ = 0.91 ± 0.12 mm), and the smallest visible vessel diameter (0.70 ± 0.11 mm). These results outperformed CE-MRA (Gd), CTA, and TOF-MRA, thus emphasizing the exceptional imaging quality of PUSIONPs in enhancing vessel contrast, delineating boundaries, and visualizing smaller vessels.

3. CONCLUSION

In summary, the application of PUSIONPs as a contrast agent for MRA demonstrated promising potential in vascular imaging. Across diverse animal models—from rabbits to beagle dogs and Bama minipigs—PUSIONP-enhanced MRA exhibited superior imaging capabilities, offering significantly heightened vascular contrast, clearer vascular boundaries, and enhanced vessel resolution compared to conventional Magnevist-enhanced MRA, Ultravist-enhanced CTA, and TOF-MRA. These characteristics highlight the capacity of PUSIONPs to enable precise microvessel visualization, thereby aiding accurate diagnoses of cardiovascular diseases. More importantly, the prolonged circulation time within the blood pool allowed for an extended imaging window, facilitating continuous monitoring of the thrombolysis process and thereby providing crucial guidance for the formulation of effective clinical treatment strategies. These findings underscore the promising clinical value of PUSIONPs as an advanced contrast agent, potentially revolutionizing cardiovascular imaging. Furthermore, owing to their capacity for targeted delivery through surface modifications, PUSIONPs hold promise beyond diagnostic imaging. They can also function as effective carriers for targeted drug delivery, with applications spanning various biomedical fields.[48,49] Looking ahead, PUSIONPs are poised to play a pivotal role in advancing personalized medicine and transforming the landscape of integrated medical care.

4. EXPERIMENTAL SECTION

4.1. Materials. PEGylated ultrasmall iron oxide nanoparticles (PUSIONPs) were supplied by Suzhou Xinying Biomedical Technology Co., Ltd. $Na^{99m}TcO_4$ was purchased from Shanghai GMS Pharmaceutical Co., Ltd. Tin(II) chloride dihydrate was purchased from Alfa Aesar Chemical Co., Ltd. Pelltobarbitalum Natricum was acquired from Shanghai Sigma-Aldrich Trading Co., Ltd. Sodium chloride solution (0.9%) was procured from Dalian Otsuka Pharmaceutical Co., Ltd. Gadopentetate Glucosamine (Gd-DTPA) and Iopromide (Ultravist) were obtained from Bayer Healthcare Ltd. Ferric chloride hexahydrate ($FeCl_3$) was provided by Shanghai Macklin Biochemical Co., Ltd. Recombinant tissue-type plasminogen activator (rt-PA) was purchased from Boehringer Ingelheim Shanghai Pharmaceuticals Co., Ltd.

4.2. Synthesis and Characterization of PEG-Coated Fe_3O_4 Nanoparticles. The morphology of PUSIONPs was characterized using transmission electron microscopy (TEM, Talos F200S G2) at an acceleration voltage of 200 kV. The hydrodynamic size of PUSIONPs was measured using a Malvern Zetasizer Nano ZS90. The relativity measurements were conducted using a 3 T animal MRI scanner (MRS 3000, MR Solutions, Guildford, UK).

4.3. Animals for the *In Vivo* Imaging Experiment. The study was conducted according to the Guidelines for the Care and Use of Laboratory Animals of the Department of Laboratory Animal Science, Soochow University, and the protocol was approved by the Ethics Committee of Soochow University. All New Zealand rabbits (2.5 kg) were purchased from Zhenghu (Jiangsu, China). Beagles (female, 5–10 kg) and Bama minipigs (female, 10–15 kg) were obtained from Agan Biotechnology Co., Ltd. (Shanghai, China).

4.4. Blood Circulation Analysis of PUSIONPs in Rabbits. ^{99m}Tc-labeled PUSIONPs were synthesized following a previous report.[50] Rabbits were intravenously administered 0.1 mmol/kg ^{99m}Tc-labeled PUSIONPs via the marginal ear vein, where an indwelling catheter was placed for repeated blood sampling. Blood samples (approximately 0.5 mL each) were collected at designated time points postinjection (1, 5, 10, 20, 30, 60, 90, 120, 240, 360, 480, 1200, and 1440 min) through the catheter. After each collection, 0.5 mL of heparinized saline was injected to prevent coagulation. The blood samples were weighed, and their radioactivity was quantified using a gamma counter to determine the blood circulation half-life of the nanoparticles.

4.5. Establishment of the Carotid Thrombosis Model. The rabbits were anesthetized with 3% pentobarbital sodium (30 mg/kg). Using a midline incision, one side of the common carotid artery was isolated, and external application of filter paper soaked with 10% $FeCl_3$ solution followed. An incompletely blocked thrombus was observed forming on the wall of the common carotid artery 20 min after induction.

https://doi.org/10.1021/acsnano.4c13356
ACS Nano 2025, 19, 3519–3530

4.6. *In Vivo* MRA/CTA Imaging of Rabbits Vessel and Carotid Artery Thrombolysis. For the evaluation of the vascular enhancement effect of the PUSIONPs contrast agent, TOF-MRA, CE-MRA, and CTA images were acquired after the rabbits were anesthetized with 3% pentobarbital sodium (30 mg/kg). Prior to the administration of contrast, a TOF-MRA and a 3D Flash sequence imaging on the rabbit head and neck were performed. Then, the contrast agent was administered through an indwelling needle into the auricular veins of the rabbits. PUSIONPs and Gd-DTPA contrast agents were infused at the recommended Gd-DTPA dose of 0.1 mmol/kg at a speed of 1 mL/s. Following this, the same sequences of scans mentioned above were repeated at 13.2 s, 1 h, 2 h, and 4 h post-injection. Afterward, CTA imaging was carried out on the head and neck of the rabbits before and after intravenous Ultravist injection at the ear margin (13.2 s, 1 h, 2 h, and 4 h). Of these, the Ultravist injection was administered via an indwelling needle (iodine concentration of 370 mg/mL and 1 mL/kg) at a rate of 1 mL/s.

For *in vivo* thrombolytic monitoring of PUSIONPs, rabbits were anesthetized with 3% pentobarbital sodium (30 mg/kg) and TOF-MRA, CE-MRA, and CTA images were acquired before and after intravenous injection of rt-PA at different time points (1, 2, 3, and 4 h). Of these, before the injection of rt-PA, PUSIONPs and Gd-DTPA contrast agents were administered to obtain CE-MRA (Fe) and CE-MRA (Gd) images, respectively, and then CTA images were collected before and after Ultravist injection, referred to as pre and 0 h. Notably, the Gd-GTPA and Ultravist were reinjected at 4 h.

The specific MRI scan sequence and parameters used for the above study are as follows: for the CE-MRA scan, a clinical MRI 64-channel head/neck coil was utilized with a 3D-Flash sequence, along with the following scanning parameters: TR = 4.78 ms, TE = 1.82 ms, FOV = 280 × 280 mm^2, matrix = 467 × 467, and FA = 20°. For the TOF-MRA imaging, it was conducted utilizing a 64-channel head and neck MRI coil within a clinical setting. The scanning parameters comprised a 3D-TOF sequence, with TR = 24 ms, TE = 3.69 ms, FOV = 220 × 220 mm^2, matrix = 367 × 367, and FA = 18°.

CTA imaging scanning parameters are as follows : voltage = 120 kV, electricity = auto mAs, thickness = 0.6 mm, and slice gap = 0.3 mm.

4.7. *In Vivo* MRA/CTA Imaging of Beagle Dogs Vessel. For the evaluation of the vascular imaging potential of PUSIONPs, the beagles were subjected to 24 h of fasting and 8 h of dehydration prior to the experiment. An indwelling 26G needle was inserted into the upper limb vein of the animals, followed by the administration of a 3% sodium pentobarbital solution (1 mL/kg) through the same needle. After anesthetization, the beagles were placed in a magnetic resonance scanning bed. CE-MRA and CTA images of the canine head and neck were acquired before and after the administration of the appropriate contrast agents. In addition, TOF-MRA images were performed.

The parameters used for the image acquisition were as follows: 3D-Flash sequence with TR = 4.0 ms, TE = 1.5 ms, FOV = 460 × 460 mm^2, matrix = 467 × 467, FA = 20°; TOF-MRA with TR = 24 ms, TE = 3.69 ms, FOV = 360 × 360 mm^2, matrix = 367 × 367, FA = 18°; CTA with voltage = 120 kV, electricity = auto mAs, thickness = 0.6 mm, and slice gap = 0.3 mm.

4.8. *In Vivo* MRA/CTA Imaging of Bama Minipigs Vessel. The pigs underwent a 24 h fast and were not allowed access to water for 8 h prior to the experiment. To prevent excessive secretion of salivary glands and asphyxiation, atropine (0.05 mg/kg) was injected. After a 15 min interval, the pigs were anesthetized with postauricular intramuscular anesthesia using Sultai 50 (10 mg/kg) mixed with Lupronin (2 mg/kg). Subsequently, the CE-MRA (Fe), CE-MRA (Gd), and CTA images were collected before and after injecting PUSIONPs, Gd-DTPA, and Ultravist via the ear vein. Subsequently, the identical sequence of scans as explained earlier was carried out at different time points. Additionally, TOF-MRA images were obtained.

The specific measurement parameters were set as follows: CE-MRA images were obtained using 64-channel head/neck coil and 3D-FLASH sequence with TR = 4.11 ms, TE = 1.61 ms, FOV = 220 × 220 mm^2, matrix = 352 × 352, and FA = 22°; TOF-MRA images were collected using 3D-TOF sequence with TR = 30 ms, TE = 3.69 ms, FOV = 220 × 220 mm^2, matrix = 352 × 352, FA = 18°; CTA images were conducted with voltage = 120 kV, electricity = auto mAs, thickness = 0.6 mm, and slice gap = 0.3 mm.

4.9. Statistical Analysis. Continuous variables are presented as the mean ± standard deviation (SD). Significant differences between groups were determined using an unpaired *t*-test (for two groups) and one-way analysis of variance (for >2 groups). In every case, a *p*-value below 0.05 was considered statistically significant (*$p < 0.05$; **$p < 0.01$; ***$p < 0.001$; ns: no significance). All magnetic resonance images were measured using the RadiAnt DICOM Viewer (64-bit), while all CT data were analyzed using software (ADW4.6, GE Healthcare) provided by the scanner manufacturer. Contrast-to-noise ratio (CNR): $CNR_{vessel} = (SI_{vessel} - SI_{tissue})/\sigma_{tissue}$, where SI_{vessel} and SI_{tissue} represent the standardized signal intensity of the vessel and surrounding tissue, respectively, and σ_{tissue} represents the standard deviation of the background signals.

ASSOCIATED CONTENT

Supporting Information

The Supporting Information is available free of charge at https://pubs.acs.org/doi/10.1021/acsnano.4c13356.

CT volume rending and axis images; Blood circulation profile of ^{99m}Tc-labeled PUSIONPs in healthy rabbits; TOF images of heathy rabbits; The schematic illustration and H and E staining of carotid common artery thrombosis model; MIP images of local complete occlusion and severe stenosis using TOF-MRA and CE-MRA (Fe); MIP images of Bama minipigs using CE-MRA(Fe), CE-MRA(Gd) and CTA; MRI signal and CT value of carotid common artery; Axial images of the ipsilateral carotid common artery and smallest vessels in Beagle dogs and Bama minipigs using CE-MRA (Fe), CE-MRA (Gd), TOF-MRA, and CTA; Table of stenosis rate change (PDF)

AUTHOR INFORMATION

Corresponding Authors

Wu Cai − *The Second Affiliated Hospital of Soochow University, Suzhou 215000, China*; Email: xwg608@126.com

Jianfeng Zeng − *Center for Molecular Imaging and Nuclear Medicine, State Key Laboratory of Radiation Medicine and Protection, School for Radiological and Interdisciplinary*

https://doi.org/10.1021/acsnano.4c13356
ACS Nano 2025, 19, 3519−3530

Sciences (RAD-X), Soochow University, Collaborative Innovation Center of Radiological Medicine of Jiangsu Higher Education Institutions, Suzhou 215123, China; orcid.org/0000-0001-7654-8724; Email: jfzeng@suda.edu.cn

Mingyuan Gao − *Center for Molecular Imaging and Nuclear Medicine, State Key Laboratory of Radiation Medicine and Protection, School for Radiological and Interdisciplinary Sciences (RAD-X), Soochow University, Collaborative Innovation Center of Radiological Medicine of Jiangsu Higher Education Institutions, Suzhou 215123, China; The Second Affiliated Hospital of Soochow University, Suzhou 215000, China; School of life Sciences, Soochow University, Suzhou 215123, China;* orcid.org/0000-0002-7360-3684; Email: gaomy@suda.edu.cn

Authors

Kuan Lu − *Center for Molecular Imaging and Nuclear Medicine, State Key Laboratory of Radiation Medicine and Protection, School for Radiological and Interdisciplinary Sciences (RAD-X), Soochow University, Collaborative Innovation Center of Radiological Medicine of Jiangsu Higher Education Institutions, Suzhou 215123, China; The Second Affiliated Hospital of Soochow University, Suzhou 215000, China*

Ruru Zhang − *Center for Molecular Imaging and Nuclear Medicine, State Key Laboratory of Radiation Medicine and Protection, School for Radiological and Interdisciplinary Sciences (RAD-X), Soochow University, Collaborative Innovation Center of Radiological Medicine of Jiangsu Higher Education Institutions, Suzhou 215123, China*

Hongzhao Wang − *Center for Molecular Imaging and Nuclear Medicine, State Key Laboratory of Radiation Medicine and Protection, School for Radiological and Interdisciplinary Sciences (RAD-X), Soochow University, Collaborative Innovation Center of Radiological Medicine of Jiangsu Higher Education Institutions, Suzhou 215123, China*

Cang Li − *Center for Molecular Imaging and Nuclear Medicine, State Key Laboratory of Radiation Medicine and Protection, School for Radiological and Interdisciplinary Sciences (RAD-X), Soochow University, Collaborative Innovation Center of Radiological Medicine of Jiangsu Higher Education Institutions, Suzhou 215123, China*

Zhe Yang − *Center for Molecular Imaging and Nuclear Medicine, State Key Laboratory of Radiation Medicine and Protection, School for Radiological and Interdisciplinary Sciences (RAD-X), Soochow University, Collaborative Innovation Center of Radiological Medicine of Jiangsu Higher Education Institutions, Suzhou 215123, China; The Second Affiliated Hospital of Soochow University, Suzhou 215000, China*

Keyang Xu − *Center for Molecular Imaging and Nuclear Medicine, State Key Laboratory of Radiation Medicine and Protection, School for Radiological and Interdisciplinary Sciences (RAD-X), Soochow University, Collaborative Innovation Center of Radiological Medicine of Jiangsu Higher Education Institutions, Suzhou 215123, China*

Xiaoyi Cao − *Center for Molecular Imaging and Nuclear Medicine, State Key Laboratory of Radiation Medicine and Protection, School for Radiological and Interdisciplinary Sciences (RAD-X), Soochow University, Collaborative Innovation Center of Radiological Medicine of Jiangsu Higher Education Institutions, Suzhou 215123, China*

Ning Wang − *Center for Molecular Imaging and Nuclear Medicine, State Key Laboratory of Radiation Medicine and Protection, School for Radiological and Interdisciplinary Sciences (RAD-X), Soochow University, Collaborative Innovation Center of Radiological Medicine of Jiangsu Higher Education Institutions, Suzhou 215123, China*

Complete contact information is available at: https://pubs.acs.org/10.1021/acsnano.4c13356

Author Contributions

#K.L. and R.Z. contributed equally. The manuscript was written through contributions of all authors. All authors have given approval to the final version of the manuscript.

Notes

The authors declare no competing financial interest.

ACKNOWLEDGMENTS

This research was funded by the National Natural Science Foundation of China (82130059, 82222033, 82172003), the Project of Suzhou Health Talent (GSWS2021025), Technological Innovation Project of CNNC Medical Industry Co. Ltd. (ZHYLYB2021006), Project of Nuclear Technology Medical Application Supported by Discipline Construction of Second Affiliated Hospital of Soochow University (XKTJ-HRC20210010), Project of State Key Laboratory of Radiation Medicine and Protection, Soochow University (GZK12024025, 1202136), and Priority Academic Program Development of Jiangsu Higher Education Institutions (PAPD).

REFERENCES

(1) Mensah, G. A.; Roth, G. A.; Fuster, V. The Global Burden of Cardiovascular Diseases and Risk Factors: 2020 and Beyond. *J. Am. Coll. Cardiol.* **2019**, *74*, 2529−2532.

(2) The Writing Committee of the Report on Cardiovascular Health and Diseases in China. Report on Cardiovascular Health and Diseases in China 2021: An Updated Summary. *Biomed. Environ. Sci.* **2022**, *35*, 573−603.

(3) Benjamin, E. J.; Muntner, P.; Alonso, A.; Bittencourt, M. S.; Callaway, C. W.; Carson, A. P.; Chamberlain, A. M.; Chang, A. R.; Cheng, S.; Das, S. R.; et al. Heart Disease and Stroke Statistics—2019 Update: A Report From the American Heart Association. *Circulation* **2019**, *139*, No. e56−e528.

(4) Perry, A. S.; Dooley, E. E.; Master, H.; Spartano, N. L.; Brittain, E. L.; Pettee Gabriel, K. Physical Activity over the Lifecourse and Cardiovascular Disease. *Circ. Res.* **2023**, *132*, 1725−1740.

(5) Roth, G. A.; Mensah, G. A.; Johnson, C. O.; Addolorato, G.; Ammirati, E.; Baddour, L. M.; Barengo, N. C.; Beaton, A. Z.; Benjamin, E. J.; Benziger, C. P.; Bonny, A.; Brauer, M.; Brodmann, M.; Cahill, T. J.; Carapetis, J.; Catapano, A. L.; Chugh, S. S.; Cooper, L. T.; Coresh, J.; Criqui, M. Global Burden of Cardiovascular Diseases and Risk Factors, 1990−2019: Update from the Gbd 2019 Study. *J. Am. Coll. Cardiol.* **2020**, *76*, 2982−3021.

(6) Stark, K.; Massberg, S. Interplay between Inflammation and Thrombosis in Cardiovascular Pathology. *Nat. Rev. Cardiol.* **2021**, *18*, 666−682.

(7) Yu, Y. J.; Xiong, W. Tirofiban Combined with rt-PA Intraarterial Thrombolysis Improves the Recanalization Rate of Acute Middle Cerebral Artery Occlusion in Rabbits. *Eur. Rev. Med. Pharmacol. Sci.* **2018**, *22*, 2888−2895.

(8) Tsivgoulis, G.; Katsanos, A. H.; Sandset, E. C.; Turc, G.; Nguyen, T. N.; Bivard, A.; Fischer, U.; Khatri, P. Thrombolysis for Acute Ischaemic Stroke: Current Status and Future Perspectives. *Lancet Neurol.* **2023**, *22*, 418−429.

(9) Powers, W. J.; Rabinstein, A. A.; Ackerson, T.; Adeoye, O. M.; Bambakidis, N. C.; Becker, K.; Biller, J.; Brown, M.; Demaerschalk, B. M.; Hoh, B.; et al. Guidelines for the Early Management of Patients with Acute Ischemic Stroke: 2019 Update to the 2018 Guidelines for the Early Management of Acute Ischemic Stroke: A Guideline for Healthcare Professionals from the American Heart Association/American Stroke Association. *Stroke* **2019**, *50*, No. e344−e418.
(10) Winzer, S.; Rickmann, H.; Kitzler, H.; Abramyuk, A.; Krogias, C.; Strohm, H.; Barlinn, J.; Pallesen, L. P.; Siepmann, T.; Arnold, S.; Moennings, P.; Mudra, H.; Linn, J.; Reichmann, H.; Weiss, N.; Gahn, G.; Alexandrov, A.; Puetz, V.; Barlinn, K. Ultrasonography Grading of Internal Carotid Artery Disease: Multiparametric German Society of Ultrasound in Medicine (Degum) Versus Society of Radiologists in Ultrasound (Sru) Consensus Criteria. *Ultraschall Med.* **2022**, *43*, 608−613.
(11) Lin, L.; Ba, Z.; Tian, H.; Qin, H.; Chen, X.; Zhou, X.; Zhao, S.; Li, L.; Xue, F.; Li, H.; et al. Ultrasound-Responsive Theranostic Platform for the Timely Monitoring and Efficient Thrombolysis in Thrombi of Tpa Resistance. *Nat. Commun.* **2024**, *15*, 6610.
(12) Collet, C.; Onuma, Y.; Andreini, D.; Sonck, J.; Pompilio, G.; Mushtaq, S.; La Meir, M.; Miyazaki, Y.; de Mey, J.; Gaemperli, O.; et al. Coronary Computed Tomography Angiography for Heart Team Decision-Making in Multivessel Coronary Artery Disease. *Eur. Heart J.* **2018**, *39*, 3689−3698.
(13) Shi, Z.; Miao, C.; Schoepf, U. J.; Savage, R. H.; Dargis, D. M.; Pan, C.; Chai, X.; Li, X. L.; Xia, S.; Zhang, X.; et al. A Clinically Applicable Deep-Learning Model for Detecting Intracranial Aneurysm in Computed Tomography Angiography Images. *Nat. Commun.* **2020**, *11*, 6090.
(14) Tian, X.; Tian, B.; Shi, Z.; Wu, X.; Peng, W.; Zhang, X.; Malhotra, A.; Mossa-Basha, M.; Sekhar, L.; Liu, Q.; Lu, J.; Hu, C.; Zhu, C. Assessment of Intracranial Atherosclerotic Plaques Using 3d Black-Blood Mri: Comparison with 3d Time-of-Flight Mra and Dsa. *J. Magn. Reson. Imaging* **2021**, *53*, 469−478.
(15) Wang, J.; Fu, D.; Tang, C.; Shu, G.; Zhang, X.; Zhang, X.; Pan, J.; Sun, S. K. Bismuth Chelate-Mediated Digital Subtraction Angiography. *Adv. Healthcare Mater.* **2024**, *13*, 2401693.
(16) Zhang, J.; Ding, S.; Zhao, H.; Sun, B.; Li, X.; Zhou, Y.; Wan, J.; Degnan, A. J.; Xu, J.; Zhu, C. Evaluation of Chronic Carotid Artery Occlusion by Non-Contrast 3d-Merge Mr Vessel Wall Imaging: Comparison with 3d-Tof-Mra, Contrast-Enhanced Mra, and Dsa. *Eur. Radiol.* **2020**, *30*, 5805−5814.
(17) Golemati, S.; Cokkinos, D. D. Recent Advances in Vascular Ultrasound Imaging Technology and Their Clinical Implications. *Ultrasonics* **2022**, *119*, 106599.
(18) Chen, W.; Cormode, D. P.; Fayad, Z. A.; Mulder, W. J. M. Nanoparticles as Magnetic Resonance Imaging Contrast Agents for Vascular and Cardiac Diseases. *WIREs Nanomed. Nanobi.* **2011**, *3*, 146−161.
(19) Shu, G.; Zhao, L.; Li, F.; Jiang, Y.; Zhang, X.; Yu, C.; Pan, J.; Sun, S. K. Metallic Artifacts-Free Spectral Computed Tomography Angiography Based on Renal Clearable Bismuth Chelate. *Biomaterials* **2024**, *305*, 122422.
(20) Su, T. H.; Hsieh, C. H.; Chan, Y. L.; Wong, Y. C.; Kuo, C. F.; Li, C. H.; Lee, C. C.; Chen, H. Y. Intravenous Ct Contrast Media and Acute Kidney Injury: A Multicenter Emergency Department-Based Study. *Radiology* **2021**, *301*, 571−581.
(21) Vassaux, G.; Zwarthoed, C.; Signetti, L.; Guglielmi, J.; Compin, C.; Guigonis, J.-M.; Juhel, T.; Humbert, O.; Benisvy, D.; Pourcher, T.; Cambien, B. Iodinated Contrast Agents Perturb Iodide Uptake by the Thyroid Independently of Free Iodide. *J. Nucl. Med.* **2018**, *59*, 121−126.
(22) Yucel, E. K.; Anderson, C. M.; Edelman, R. R.; Grist, T. M.; Baum, R. A.; Manning, W. J.; Culebras, A.; Pearce, W. Magnetic Resonance Angiography. *Circulation* **1999**, *100*, 2284−2301.
(23) Wang, J.; Han, B.; Ma, M.; Zhao, Y.; Li, B.; Zhou, J.; Wu, C.; Zhang, X.; Pan, J.; Sun, S. K. Magnetic Resonance Angiography with Hour-Scale Duration after Single Low-Dose Administration of Biocompatible Gadolinium Oxide Nanoprobe. *Adv. Healthcare Mater.* **2024**, *13*, 2303389.
(24) Pierot, L.; Portefaix, C.; Boulin, A.; Gauvrit, J.-Y. Follow-up of Coiled Intracranial Aneurysms: Comparison of 3d Time-of-Flight and Contrast-Enhanced Magnetic Resonance Angiography at 3t in a Large, Prospective Series. *Eur. Radiol.* **2012**, *22*, 2255−2263.
(25) Shi, Z.; Zhao, X.; Zhu, S.; Miao, X.; Zhang, Y.; Han, S.; Wang, B.; Zhang, B.; Ye, X.; Dai, Y.; Chen, C.; Rao, S.; Lin, J.; Zeng, M.; Wang, H. Time-of-Flight Intracranial Mra at 3 T Versus 5 T Versus 7 T: Visualization of Distal Small Cerebral Arteries. *Radiology* **2023**, *306*, 207−217.
(26) Hartung, M. P.; Grist, T. M.; François, C. J. Magnetic Resonance Angiography: Current Status and Future Directions. *J. Cardiovasc. Magn. Reson.* **2011**, *13*, 19.
(27) De León-Rodríguez, L. M.; Martins, A. F.; Pinho, M. C.; Rofsky, N. M.; Sherry, A. D. Basic Mr Relaxation Mechanisms and Contrast Agent Design. *J. Magn. Reson. Imaging* **2015**, *42*, 545−565.
(28) Wang, J.; Jia, Y.; Wang, Q.; Liang, Z.; Han, G.; Wang, Z.; Lee, J.; Zhao, M.; Li, F.; Bai, R.; et al. An Ultrahigh-Field-Tailored T 1 − T 2 Dual-Mode MRI Contrast Agent for High-Performance Vascular Imaging. *Adv. Mater.* **2021**, *33*, 2004917.
(29) Anzalone, N.; Scomazzoni, F.; Cirillo, M.; Cadioli, M.; Iadanza, A.; Kirchin, M. A.; Scotti, G. Follow-up of Coiled Cerebral Aneurysms: Comparison of Three-Dimensional Time-of-Flight Magnetic Resonance Angiography at 3 T with Three-Dimensional Time-of-Flight Magnetic Resonance Angiography and Contrast-Enhanced Magnetic Resonance Angiography at 1.5 T. *Invest. Radiol.* **2008**, *43*, 559−567.
(30) Zhou, Z.; Lu, Z. R. Gadolinium-Based Contrast Agents for Magnetic Resonance Cancer Imaging. *WIREs Nanomed. Nanobi.* **2013**, *5*, 1−18.
(31) Kanda, T.; Fukusato, T.; Matsuda, M.; Toyoda, K.; Oba, H.; Kotoku, J.; Haruyama, T.; Kitajima, K.; Furui, S. Gadolinium-Based Contrast Agent Accumulates in the Brain Even in Subjects without Severe Renal Dysfunction: Evaluation of Autopsy Brain Specimens with Inductively Coupled Plasma Mass Spectroscopy. *Radiology* **2015**, *276*, 228−232.
(32) Gulani, V.; Calamante, F.; Shellock, F. G.; Kanal, E.; Reeder, S. B. International Society for Magnetic Resonance in, M. Gadolinium Deposition in the Brain: Summary of Evidence and Recommendations. *Lancet Neurol.* **2017**, *16*, 564−570.
(33) Weng, Q.; Hu, X.; Zheng, J.; Xia, F.; Wang, N.; Liao, H.; Liu, Y.; Kim, D.; Liu, J.; Li, F.; He, Q.; Yang, B.; Chen, C.; Hyeon, T.; Ling, D. Toxicological Risk Assessments of Iron Oxide Nanocluster- and Gadolinium-Based T1mri Contrast Agents in Renal Failure Rats. *ACS Nano* **2019**, *13*, 6801−6812.
(34) Lee, N.; Hyeon, T. Designed Synthesis of Uniformly Sized Iron Oxide Nanoparticles for Efficient Magnetic Resonance Imaging Contrast Agents. *Chem. Soc. Rev.* **2012**, *41*, 2575−2589.
(35) Daldrup-Link, H. E. Ten Things You Might Not Know About Iron Oxide Nanoparticles. *Radiology* **2017**, *284*, 616−629.
(36) Wang, S.; Li, J.; Chen, L.; Zeng, J.; Gao, M. Fe(2+)-Dominated Relaxometric Properties of Iron Oxide Nanoparticles as Mri Contrast Agents. *J. Phys. Chem. Lett.* **2024**, *15*, 8861−8866.
(37) Arami, H.; Khandhar, A.; Liggitt, D.; Krishnan, K. M. In Vivo Delivery, Pharmacokinetics, Biodistribution and Toxicity of Iron Oxide Nanoparticles. *Chem. Soc. Rev.* **2015**, *44*, 8576−8607.
(38) Dadfar, S. M.; Roemhild, K.; Drude, N. I.; von Stillfried, S.; Knuchel, R.; Kiessling, F.; Lammers, T. Iron Oxide Nanoparticles: Diagnostic, Therapeutic and Theranostic Applications. *Adv. Drug Delivery Rev.* **2019**, *138*, 302−325.
(39) Li, C.; Shan, S.; Chen, L.; Afshari, M. J.; Wang, H.; Lu, K.; Kou, D.; Wang, N.; Gao, Y.; Liu, C.; et al. Using Adaptive Imaging Parameters to Improve Pegylated Ultrasmall Iron Oxide Nanoparticles-Enhanced Magnetic Resonance Angiography. *Adv. Sci.* **2024**, *11*, No. e2405719.
(40) Zhou, D.; Shan, S.; Chen, L.; Li, C.; Wang, H.; Lu, K.; Ge, J.; Wang, N.; Afshari, M. J.; Zhang, Y.; et al. Trapped in Endosome Pegylated Ultra-Small Iron Oxide Nanoparticles Enable Extraordi-

https://doi.org/10.1021/acsnano.4c13356
ACS Nano 2025, 19, 3519−3530

narily High Mr Imaging Contrast for Hepatocellular Carcinomas. *Adv. Sci.* **2024**, *11*, No. e2401351.
(41) Chen, C.; Ge, J.; Gao, Y.; Chen, L.; Cui, J.; Zeng, J.; Gao, M. Ultrasmall Superparamagnetic Iron Oxide Nanoparticles: A Next Generation Contrast Agent for Magnetic Resonance Imaging. *Wiley Interdiscip. Rev.: Nanomed. Nanobiotechnol.* **2022**, *14*, e1740.
(42) Shin, T. H.; Kim, P. K.; Kang, S.; Cheong, J.; Kim, S.; Lim, Y.; Shin, W.; Jung, J. Y.; Lah, J. D.; Choi, B. W.; Cheon, J. High-Resolution T(1) Mri Via Renally Clearable Dextran Nanoparticles with an Iron Oxide Shell. *Nat. Biomed. Eng.* **2021**, *5*, 252−263.
(43) Jeon, M.; Halbert, M. V.; Stephen, Z. R.; Zhang, M. Iron Oxide Nanoparticles as T1 Contrast Agents for Magnetic Resonance Imaging: Fundamentals, Challenges, Applications, and Prospectives. *Adv. Mater* **2021**, *33*, 1906539.
(44) Zhang, R.; Lu, K.; Xiao, L.; Hu, X.; Cai, W.; Liu, L.; Liu, Y.; Li, W.; Zhou, H.; Qian, Z.; et al. Exploring Atherosclerosis Imaging with Contrast-Enhanced Mri Using Pegylated Ultrasmall Iron Oxide Nanoparticles. *Front. Bioeng. Biotechnol.* **2023**, *11*, 1279446.
(45) Wang, H.; Jiang, Q.; Shen, Y.; Zhang, L.; Haacke, E. M.; Ge, Y.; Qi, S.; Hu, J. The Capability of Detecting Small Vessels Beyond the Conventional Mri Sensitivity Using Iron-Based Contrast Agent Enhanced Susceptibility Weighted Imaging. *NMR Biomed.* **2020**, *33*, No. e4256.
(46) Wei, R.; Cai, Z.; Ren, B. W.; Li, A.; Lin, H.; Zhang, K.; Chen, H.; Shan, H.; Ai, H.; Gao, J. Biodegradable and Renal-Clearable Hollow Porous Iron Oxide Nanoboxes for in Vivo Imaging. *Chem. Mater.* **2018**, *30*, 7950−7961.
(47) Lu, Y.; Xu, Y. J.; Zhang, G. B.; Ling, D.; Wang, M. Q.; Zhou, Y.; Wu, Y. D.; Wu, T.; Hackett, M. J.; Hyo Kim, B.; Chang, H.; Kim, J.; Hu, X. T.; Dong, L.; Lee, N.; Li, F.; He, J. C.; Zhang, L.; Wen, H. Q.; Yang, B. Iron Oxide Nanoclusters for T (1) Magnetic Resonance Imaging of Non-Human Primates. *Nat. Biomed. Eng.* **2017**, *1*, 637−643.
(48) Low, L. E.; Lim, H. P.; Ong, Y. S.; Siva, S. P.; Sia, C. S.; Goh, B. H.; Chan, E. S.; Tey, B. T. Stimuli-Controllable Iron Oxide Nanoparticle Assemblies: Design, Manipulation and Bio-Applications. *J. Controlled Release* **2022**, *345*, 231−274.
(49) Qiao, R.; Fu, C.; Forgham, H.; Javed, I.; Huang, X.; Zhu, J.; Whittaker, A. K.; Davis, T. P. Magnetic Iron Oxide Nanoparticles for Brain Imaging and Drug Delivery. *Adv. Drug Delivery Rev.* **2023**, *197*, 114822.
(50) Chen, L.; Gao, Y.; Ge, J.; Zhou, Y.; Yang, Z.; Li, C.; Huang, B.; Lu, K.; Kou, D.; Zhou, D.; Chen, C.; Wang, S.; Wu, S.; Zeng, J.; Huang, G.; Gao, M. A Clinically Translatable Kit for MRI/NMI Dual-Modality Nanoprobes Based on Anchoring Group-Mediated Radiolabeling. *Nanoscale* **2023**, *15*, 3991−3999.

https://doi.org/10.1021/acsnano.4c13356
ACS Nano 2025, 19, 3519−3530